The Astrophysical Journal, 992:67 (13pp), 2025 October 10 https://doi.org/10.3847/1538-4357/ae00c5

Impact of Cosmic Ray-driven Outflows on Lyα Emission in Cosmological Simulations

Taysun Kimm[1], Julien Devriendt[2], Francisco Rodríguez Montero[2,3], Adrianne Slyz[2], Jérémy Blaizot[4], Harley Katz[3,5], Beomchan Koh[1], and Hyunmi Song[6]

[1] Department of Astronomy, Yonsei University, 50 Yonsei-ro, Seodaemun-gu, Seoul 03722, Republic of Korea; tkimm@yonsei.ac.kr
[2] Astrophysics, University of Oxford, Denys Wilkinson Building, Keble Road, Oxford OX1 3RH, UK
[3] Department of Astronomy & Astrophysics, University of Chicago, 5640 S Ellis Avenue, Chicago, IL 60637, USA
[4] Univ Lyon, Univ Lyon1, Ens de Lyon, CNRS, Centre de Recherche Astrophysique de Lyon UMR5574, F-69230 Saint-Genis-Laval, France
[5] Kavli Institute for Cosmological Physics, University of Chicago, Chicago, IL 60637, USA
[6] Department of Astronomy and Space Science, Chungnam National University, Daejeon 34134, Republic of Korea

Received 2025 July 14; revised 2025 August 19; accepted 2025 August 27; published 2025 October 7

Abstract

Cosmic ray (CR) feedback has been proposed as a powerful mechanism for driving warm gas outflows in galaxies. We use cosmological magnetohydrodynamic simulations to investigate the impact of CR feedback on neutral hydrogen (H I) in a $10^{11}\,M_{\odot}$ dark matter halo at $2 < z < 4$. To this end, we postprocess the simulations with ionizing radiative transfer and perform Monte Carlo Lyman-α (Lyα) transfer calculations. CR feedback reduces H I column densities around young stars, thereby allowing more Lyα photons to escape and consequently offering a better match to the Lyα luminosities of observed Lyα emitters. Although galaxies with CR-driven outflows have more extended H I in the circumgalactic medium, two Lyα line properties sensitive to optical depth and gas kinematic—the location of the red peak relative to the Lyα line center in velocity space ($v_{\rm red}$) and relative strength of the blue-to-red peaks (B/R)—cannot distinguish between the CR-driven and non-CR simulations. This is because Lyα photons propagate preferentially along low H I density channels created by the ionizing radiation, thereby limiting the scattering with volume-filling H I. In contrast, the observed low flux ratios between the valley and peak and the surface brightness profiles are better reproduced in the model with CR-driven outflows because the Lyα photons interact more before escaping, rather than being destroyed by dust as is the case in the non-CR simulation. We discuss the potential cause of the paucity of sightlines in simulations that exhibit prominent red peaks and large $v_{\rm red}$, which may require the presence of more volume-filling H I.

Unified Astronomy Thesaurus concepts: Lyα galaxies (978); Stellar feedback (1602); Radiative transfer (1335)

1. Introduction

Galaxy formation models require strong gaseous outflows to explain inefficient star formation observed in the local Universe (e.g., T. Naab & J. P. Ostriker 2017). However, the driving mechanisms of these galactic outflows remain unclear. While the explosion of massive stars is considered a powerful regulator of star formation, numerical simulations have often struggled to reproduce observed galaxy properties, such as the stellar mass-to-halo mass ratio, without the explosion energy being artificially boosted (H. Li et al. 2018; J. Rosdahl et al. 2018, see P. F. Hopkins et al. 2018). Although the inclusion of UV radiation feedback can potentially lower the density into which supernova (SN) remnants propagate (S. Geen et al. 2015), radiation alone is insufficient to drive outflows exceeding several hundreds of km s^{-1}, as the neutral medium is collisionally ionized rapidly before it is accelerated. nonthermal pressure from multi-scattered infrared (e.g., N. Murray et al. 2005; P. F. Hopkins et al. 2011) or Lyman-α (Lyα) photons (e.g., A. Smith et al. 2017; T. Kimm et al. 2018; O. Nebrin et al. 2025) is also suggested as an effective mechanism to launch winds in dusty or dust-free regions, respectively. However, the number of scatterings is highly sensitive to the medium's geometry and velocity structures (M. A. Skinner & E. C. Ostriker 2015; M. Gronke & M. Dijkstra 2016), thereby rendering the nonthermal radiation pressure a less robust solution to the overcooling problem, which occurs in diverse environments. It is also possible that multiple processes operate simultaneously, but the effects of stellar feedback generally become weakened with increasing density (e.g., J.-G. Kim et al. 2023), thus making it susceptible to radiative losses.

To prevent runaway cooling and regulate star formation, an energy source effective at high densities ($n_{\rm H} \gtrsim 100\,{\rm cm}^{-3}$) is required. One promising candidate is the nonthermal pressure support from cosmic rays (CRs), which can be generated across shocks driven by SNe or active galactic nuclei via diffusive shock acceleration. Owing to its relativistic nature, CR pressure decays more slowly than does the thermal pressure of an ideal gas. The additional support from CRs in the galactic midplane is known to drive gentle, warm outflows with temperatures on the order of 10^{4-5} K (P. Girichidis et al. 2016; M. Ruszkowski et al. 2017), which are absent in the canonical interstellar medium (ISM), wherein thermal instability rapidly removes such gas. Early studies assuming a constant CR diffusion coefficient show that stronger outflows reduce the star formation rates by a small factor in isolated disk galaxies (M. Salem & G. L. Bryan 2014; T. K. Chan et al. 2019; G. Dashyan & Y. Dubois 2020; V. A. Semenov et al. 2021; M. Farcy et al. 2022). M. Farcy et al. (2025) further show that gas displaced by CR feedback fills the low-density channels, thereby increasing the optical depth to Lyman continuum (LyC) photons and thus delaying reionization of the universe. A natural question arises as to whether CR pressure leaves observable traces in galaxies.

Historically, the stellar mass-to-halo mass relation, shape of galactic rotation curves, and chemical information have been useful probes of galaxy formation (to name a few, P. F. Hopkins et al. 2018; R. Davé et al. 2019; D. Nelson et al. 2019; O. Agertz et al. 2021; Y. Dubois et al. 2021). Confronting the mass loading of galactic outflows is another useful approach (S. Veilleux et al. 2005; V. Pandya et al. 2021); however, detailed modeling of spectroscopic line formation is required for a direct comparison with observations (C. B. Hummels et al. 2017; V. Mauerhofer et al. 2021). Alternatively, spectroscopic signatures in quasar absorption lines can be used to infer hydrogen or metal column densities in the circumgalactic medium (CGM; J. K. Werk et al. 2013; J. X. Prochaska et al. 2017), constraining stellar feedback models. D. DeFelippis et al. (2024) show that although still insufficient, a CR model with a high diffusion coefficient $\kappa = 3 \times 10^{29}\,\mathrm{cm^2\,s^{-1}}$ can account better for the large C IV column densities observed.

Alongside the absorption features, Lyα emission provides a unique window through which the physical properties of the neutral medium can be studied. Owing to its resonant nature, Lyα emission forms a double-peaked line profile, with peak velocities mainly determined by the optical depth (M. Dijkstra 2014; B.-X. Lao & A. Smith 2020), and the separation of the double peak $v_{\rm sep}$ given by

$$v_{\rm sep} = 336\,\mathrm{km\,s^{-1}}\,\sqrt{1+\mathcal{M}^2}\;N_{20}^{1/3}\,T_4^{1/6}, \qquad (1)$$

where $\mathcal{M}$ is the Mach number, $N_{20} \equiv N_{\rm HI}/10^{20}\,\mathrm{cm^{-2}}$, $N_{\rm HI}$ is the H I column density, and $T_4 \equiv T/10^4\,\mathrm{K}$, in the case of a dust-free uniform sphere. Moreover, the relative flux ratio between the blue and red sides of the line profile (B/R) can provide information about the bulk motion of the scattering medium, as backscattering photons enhance the flux redward (or blueward) of the line center depending on whether the gas is outflowing (or inflowing) (M. Dijkstra et al. 2006; A. Verhamme et al. 2006). Analyzing the Lyα spectrum of star-forming galaxies, R. F. Trainor et al. (2015), for example, found that, at $z \sim 2$, the majority of actively star-forming galaxies exhibit $B/R < 1$, suggesting that the scattering medium around the galaxies is outflowing; this is consistent with the presence of blueshifted low-ionization metal-absorption lines (C. C. Steidel et al. 2010). The ubiquitous detection of large Lyα halos around high-z star-forming galaxies is also noteworthy (M. Rauch et al. 2008; C. C. Steidel et al. 2011; M. Hayes et al. 2013; L. Wisotzki et al. 2016, 2018; F. Leclercq et al. 2017). Using a simple 1D halo model with varying densities and velocities, H. Song et al. (2020) demonstrate that both Lyα lines and surface brightness (SB) profiles of some of the F. Leclercq et al. (2017) samples can be recovered if the halo has an extended neutral outflow. D. K. Erb et al. (2023) further show that not only the Lyα properties but also the low-ionization metal absorption lines of twelve $10^9\,M_\odot$ galaxies at $z \sim 2$ are well fitted by multiphase clumpy outflow models (see also T. Garel et al. 2024).

Because an extended CGM constitutes one of the most distinctive features of simulations with CR-driven outflows, it is interesting to investigate whether the predicted Lyα lines are significantly affected by CRs. Using stratified ISM simulations (P. Girichidis et al. 2018), M. Gronke et al. (2018) argue that the two characteristic features of Lyα emitters (LAEs)—strongly red-peaked Lyα lines with minimal flux at the line center—are better reproduced when CR pressure is included. However, the large value of the location of the red peak in velocity space ($v_{\rm red}$) is not reproduced even when CR-driven outflows are present. Given that the setup of these simulations is idealized, revisiting this issue by analyzing galaxies simulated in a cosmological environment, where discontinuous external accretion events can drive stronger outflows, is necessary. Recently, postprocessing a cosmological simulation of a halo of mass $5 \times 10^9\,M_\odot$ at $z = 3.5$, Y. Yuan et al. (2024) demonstrated that a dwarf galaxy simulated with CRs exhibits a more extended Lyα halo than the one without, thereby hinting at the importance of CR driven outflows in Lyα prediction. We build upon these studies and use recent cosmological magnetohydrodynamic simulations of a more massive halo ($10^{11}\,M_\odot$ at $z \sim 2$), run with and without CRs (F. Rodríguez Montero et al. 2024), to investigate the differences in Lyα features. We note that the simulated galaxies differ significantly in stellar mass and CGM structures, depending on the presence of CRs; this provides an interesting testbed to investigate if Lyα can be used to constrain galaxy formation models.

The remainder of this paper is structured as follows: Section 2 describes the simulations and postprocessing methods used to generate the mock Lyα spectra and images. In Section 3, we present our analysis of the Lyα properties of a simulated galaxy at different redshifts and their comparison with observed LAEs. In Section 4, we compare the simulation results with and without the ionizing radiative transfer and explore the implications and potential caveats of our interpretations. Finally, we conclude this paper with a summary and future prospects in Section 5.

2. Methods

2.1. Magnetohydrodynamic Simulations

To study Lyα line properties of high-z galaxies, we use cosmological magnetohydrodynamic simulations run with the adaptive mesh refinement (AMR) code RAMSES (R. Teyssier 2002; S. Fromang et al. 2006). The simulations use the NUT galaxy zoom-in initial condition (L. C. Powell et al. 2011), which contains a $\sim 10^{11}\,M_\odot$ dark matter halo at $z \sim 2$. Gas cools via atomic and metallic species, depending on the gas-phase metallicity, with a uniform UV background turned on at $z = 9$ (F. Haardt & P. Madau 1996). Star particles form in gravitationally unstable regions with an efficiency set by the local magneto-thermo-turbulent conditions (T. Kimm et al. 2017; S. Martin-Alvarez et al. 2020). Type II SNe of an explosion energy of 10^{51} erg are modeled using the mechanical feedback scheme (T. Kimm et al. 2015), with a rate of 0.02 $M_\odot{}^{-1}$. We assume that 10% of the SN energy is transferred to the accelerated CRs (e.g., G. Morlino & D. Caprioli 2012; D. Caprioli & A. Spitkovsky 2014). Our fiducial run includes not only anisotropic diffusion of CRs with a coefficient of $\kappa = 3 \times 10^{28}\,\mathrm{cm^2\,s^{-1}}$, but also streaming at the local Alfvén wave velocity (Y. Dubois et al. 2019). The simulations employ an initial magnetic field of 3×10^{-12} G, which amplifies to a few μG within a Gyr timescale. The dark matter and stellar mass resolution are $5.5 \times 10^4\,M_\odot$ and $4.5 \times 10^3\,M_\odot$, respectively, and the maximum AMR resolution is $\approx$23 pc (physical). A more detailed explanation of the simulations can be obtained from F. Rodríguez Montero et al. (2024).

2.2. Lyα Radiative Transfer

To compute the Lyα emission, we use the Monte Carlo radiative transfer (MCRT) code RASCAS (L. Michel-Dansac et al. 2020). A recombinative source term is calculated from the spectral energy distribution (SED) of each star particle,[7] while the abundance of hydrogen ion species from the simulations is used to calculate a collisional term (if necessary). We use the Binary Population and Spectral Synthesis code (v2, E. R. Stanway et al. 2016) to obtain the SED of each stellar particle, which is characterized by its stellar mass, metallicity, and age. Because only a small fraction of ionizing photons tends to escape from star-forming galaxies at high redshift (e.g., A. Saxena et al. 2022), we assume that all the LyC photons are absorbed by nearby neutral hydrogen, and 68% are reprocessed into Lyα.

Because the cosmological simulations are performed without fully coupled ionizing radiation transport, we postprocess the simulation outputs using RAMSES-RT (J. Rosdahl et al. 2013), and update the ionization and temperature structures (see Appendix). This significantly alters our interpretation of the results, as discussed below. For snapshots processed with RAMSES-RT, we additionally account for Lyα produced via collisional excitation, as in T. Kimm et al. (2022). Because the resolution of the simulations is finite, we ignore collisional excitation from cells, wherein the local cooling time ($t_{\rm cool}$) is underesolved, i.e., $\Delta t > t_{\rm cool}/10$ (P. D. Mitchell et al. 2021); here, Δt is the local simulation (fine) timestep. Lyα photons are then propagated, interacting with neutral hydrogen and deuterium with a ratio of $D/H = 3 \times 10^{-5}$ until they escape from the virial sphere or are destroyed by dust. We adopt a simple dust prescription, in which dust is assumed to be present in the neutral gas, with only 1% surviving in the fully ionized media (P. Laursen et al. 2009). The amount of dust is scaled to the metal mass using the dust-to-metal ratio for the Small Magellanic Cloud, inferred from the METAL program (J. Roman-Duval et al. 2022). A uniform turbulence of $20\,{\rm km\,s^{-1}}$ is assumed when calculating the Lyα interaction probabilities. We use 10^5 photon packets by default and rerun the MCRT until at least 2000 photon packets contribute to the angle-averaged emission line profile. We also generate 10 mock spectra along randomly chosen sightlines for a more direct comparison with the observations. To define the flux redward (R) or blueward (B) of the Lyα spectrum, we compute the attenuated Hα emission based on stellar particles for each angle-averaged or mock spectrum and take its flux average as the line center.

3. Results

3.1. Global Galactic Properties

The average stellar mass of the simulated galaxy is $M_\star \approx 3 \times 10^9\,M_\odot$ in the fiducial run with CR feedback at $2 \lesssim z \lesssim 4$. As discussed already in F. Rodríguez Montero et al. (2024), this is in reasonable agreement with that predicted from the stellar-to-halo mass relation derived from the halo abundance matching technique (e.g., P. S. Behroozi et al. 2013). The simulated galaxy is rotationally supported, with an average star formation rate of $\sim 4\,M_\odot\,{\rm yr^{-1}}$ and a stellar metallicity of $\approx 0.25\,Z_\odot$. The dust-attenuated UV magnitude at 1500 Å is $M_{1500} \sim -18.5$, and the UV slope measured at $1268 \leqslant \lambda/\text{Å} \leqslant 2580$ (e.g., D. Calzetti et al. 1994) is $\beta_{\rm UV} \approx -1.5$. Note that these are similar to the typical properties of the LAEs at $z \sim 3$, although the CRMHD galaxy may be at the slightly more massive end of these LAEs (e.g., E. Gawiser et al. 2007). In contrast, the MHD run (i.e., galaxy simulated without CRs) is four times more massive ($M_\star \approx 1.4 \times 10^{10}\,M_\odot$), metal-rich ($\approx 0.63\,Z_\odot$), and more actively star-forming ($\sim 8\,M_\odot\,{\rm yr^{-1}}$), but redder with $\beta_{\rm UV} \approx -1.2$. At $z = 2$, the simulated galaxy in the MHD run has a massive stellar core at the center with the maximum circular velocity reaching $370\,{\rm km\,s^{-1}}$. All of these features suggest that the MHD run suffers from overcooling (e.g., T. Kimm et al. 2015), whereas the star formation is more controlled in the CRMHD run. These two simulations, therefore, constitute a useful set to investigate whether different physical processes leave any distinct imprints on the Lyα observables. We reemphasize that this comparison is particularly intriguing because CR feedback is known to drive warm outflows, which can give rise to more extended neutral hydrogen (e.g., P. Girichidis et al. 2016; M. Farcy et al. 2022). Figure 1 indeed shows that the galaxy simulated with CRs exhibits an extended CGM with $N_{\rm HI} \sim 10^{17-18}\,{\rm cm^{-2}}$, whereas, in the MHD run, most of this gas tends to collapse directly onto the central galaxy.

In Figure 2, we compare the 1D-projected, attenuated UV magnitude at 1500 Å (M_{1500}) and Lyα luminosities with those of the observed LAE samples. Note that here we use the Lyα luminosities obtained from the snapshots after postprocessing with RAMSES-RT to make more direct comparisons with observations. Although the MHD galaxies are more actively star-forming than those in the CRMHD run, the attenuated $L_{\rm Ly\alpha}$ is $\sim$50% fainter ($\approx 3.5 \times 10^{41}\,{\rm erg\,s^{-1}}$ versus $5.3 \times 10^{41}\,{\rm erg\,s^{-1}}$), as the typical escape fraction of Lyα ($f_{\rm Ly\alpha}$) is significantly lower ($\approx$0.025 versus 0.085). Similarly, the intrinsic M_{1500} is brighter by $\approx$1 mag in the MHD run; however, the attenuated M_{1500} is comparable, as the dust attenuation is stronger in the MHD run. As a result, we find that the CRMHD samples are more compatible with the observed LAEs, whereas too little Lyα escapes from the MHD sample for a given M_{1500}. Part of this vertical offset may be alleviated by resolving the turbulent structures in the hydrodynamic simulations, as these allow a more efficient escape of Lyα photons (T. Kimm et al. 2019; K. Kakiichi & M. Gronke 2021). However, the ability to disrupt the star-forming clouds early via some collective feedback is more likely to be effective in enhancing the escape fraction, as it directly controls the low-density channels, through which Lyα escapes (e.g., T. Kimm et al. 2022). Bearing these differences in mind, we first analyze the simulations without postprocessing with RAMSES-RT and compare them with those obtained from the postprocessed snapshots.[8]

3.2. Impact of Cosmic Rays on Lyα Profiles

We begin by discussing the impact of CR pressure on H I column density distributions, which are important for Lyα radiative transfer. Figure 3 demonstrates that CR feedback not only produces an extended distribution of neutral hydrogen (Figure 1) but also lowers $N_{\rm HI}$ around young stars. Here, we measure $N_{\rm HI}$ from each star particle by casting rays along 3072

---

[7] In principle, the recombinative term can also be obtained from the ion species, but we adopt this approximation to facilitate the direct comparison between simulations with and without postprocessing of ionizing radiation transport.

[8] We discuss the results of the simulations without LyC postprocessing, because simulations with CR-driven outflows are often performed without RT. The comparison also provides insights into how observed Lyα spectra may be obtained, as discussed later.

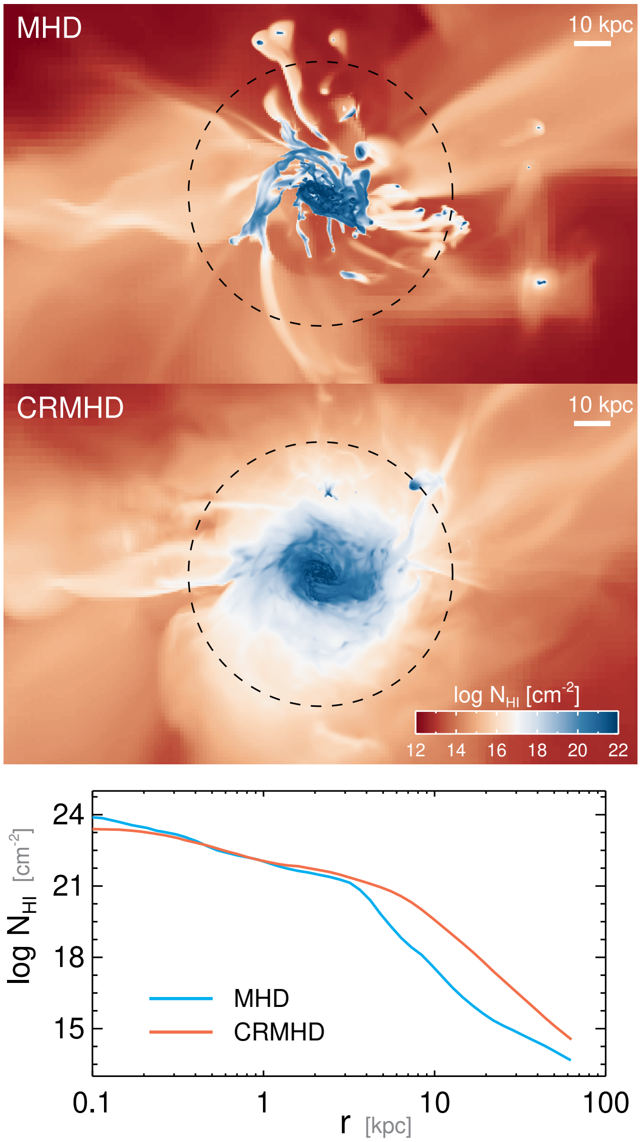

Figure 1. Distribution of neutral hydrogen column density ($N_{\rm HI}$) for the simulated halo with $3 \times 10^{11} M_\odot$ at $z \approx 2$ from the runs without and with CRs (top and middle panel, respectively). The dashed circles denote 0.5 $R_{\rm vir}$, where $R_{\rm vir}$ is the virial radius of the dark matter halo ($\approx$72 kpc). The neutral hydrogen fraction is recomputed by postprocessing each snapshot with RAMSES-RT. The bottom panel shows the azimuthally averaged $N_{\rm HI}$ profile. The galaxy simulated with CR feedback clearly has a more extended H I distribution than the one without, even though the total H I mass is smaller.

sightlines inside the virial sphere using the HEALPIX algorithm (K. M. Górski et al. 2005). The solid histograms in Figure 3 are obtained by taking LyC luminosity-weighted averages from all the snapshots over the range $2 \leqslant z \leqslant 4$ without LyC postprocessing. Stars in the `MHD` run are enshrouded by an optically thick gas of $N_{\rm HI} \sim 10^{23}\,{\rm cm}^{-2}$, whereas the values of $N_{\rm HI}$ in the `CRMHD` run are smaller by an order of magnitude (solid lines). A small upturn below $N_{\rm HI} \sim 10^{14}\,{\rm cm}^{-2}$ is present, but it accounts for less than 0.1% of the total sightlines. As can be seen from Figure 1, the reduction in $N_{\rm HI}$ due to CR feedback occurs on ISM scales, not CGM scales. When we postprocess the simulation output with RAMSES-RT to account for photo-heating by ionizing radiation (dotted–dashed lines), the ionized hydrogen fraction is increased, but the decrease in $N_{\rm HI}$ is not very significant (see also Figure A1 for a comparison of $N_{\rm HI}$ before and after LyC postprocessing). The $N_{\rm HI}$ distribution becomes more skewed to lower values after the postprocessing, but the luminosity-weighted logarithmic mean shifts only from $\log N_{\rm HI}/{\rm cm}^{-2} = 22.7$ to 22.4 in the case of `CRMHD` or from 23.4 to 23.3 in `MHD`. Thus, the H I distribution remains still more extended, and the inner halo with $r < 0.2\,R_{\rm vir}$ is filled with $N_{\rm HI} \gtrsim 10^{17}\,{\rm cm}^{-2}$ in `CRMHD`, as can be seen in Figure 1.

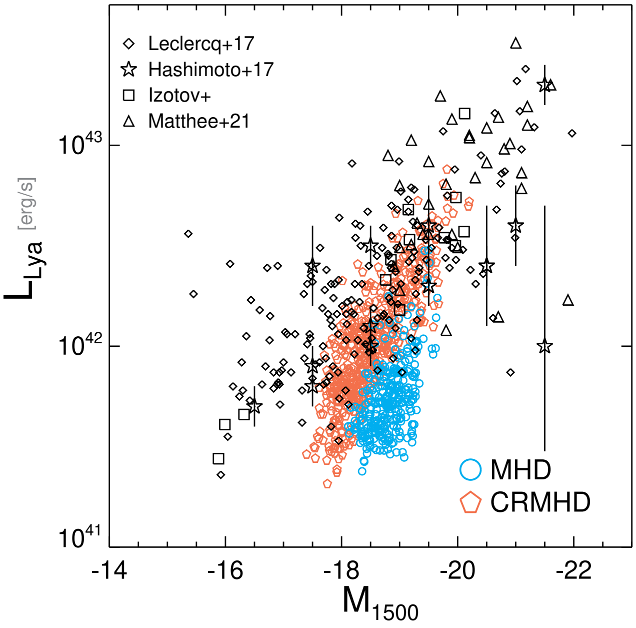

Figure 2. Comparison of the UV magnitudes at 1500 Å (M_{1500}) and Lyα properties of a simulated galaxy with observations. Black symbols indicate the observed samples of LAEs at various redshifts (T. Hashimoto et al. 2017; F. Leclercq et al. 2017; Y. I. Izotov et al. 2018a; J. Matthee et al. 2021), as indicated in the legend. Blue circles and red pentagons indicate simulated UV and Lyα from our simulations without and with CR feedback, respectively. Both quantities are dust-attenuated. Each data point represents a different sightline and snapshot between $2 \leqslant z \leqslant 4$. Intergalactic medium (IGM) attenuation, which lowers the Lyα luminosities by ~15%, is not included in this figure.

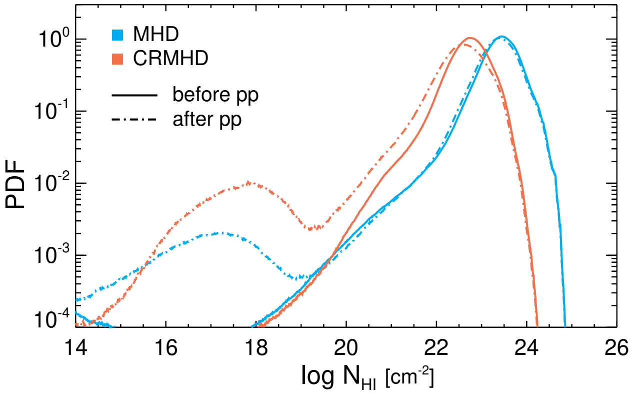

Figure 3. LyC luminosity-weighted distribution of $N_{\rm HI}$ measured from each star particle over $2 \leqslant z \leqslant 4$. Different color-codes correspond to different simulations, as shown in the legend. Simulations postprocessed with RAMSES-RT are shown as dotted–dashed lines, while those without postprocessing are shown as solid lines.

3.2.1. Peak Locations and Blue-to-Red Flux Ratios

We find that the emergent spectra of the two simulations (before LyC postprocessing) are notably different. To focus on

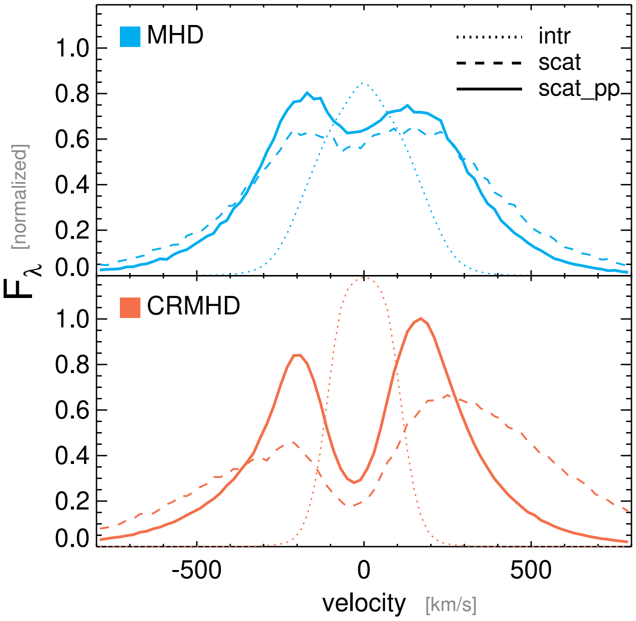

Figure 4. Stacked, angle-averaged Lyα profiles from the MHD and CRMHD runs (upper and lower panels, respectively). Profiles are normalized to the maximum flux of the emergent spectrum in the CRMHD run. Intrinsic fluxes are reduced by a factor of two for clarity. The dotted and dashed lines represent the intrinsic Lyα spectrum and results of MCRT calculations on the simulation outputs without LyC postprocessing, respectively. The solid lines indicate the MCRT calculations performed on the postprocessed simulations, which also include the contribution from collisional radiation. Attenuation by the IGM is not included.

the properties of the Lyα profiles, we compute the average of the normalized angle-averaged Lyα spectrum at $2 \lesssim z \lesssim 4$ in Figure 4. Although the typical input spectrum (dotted lines) is narrower in `CRMHD`, the angle-averaged emergent spectrum (dashed lines) is broader. The flux redward of the Lyα spectrum dominates over the blue part ($B/R \sim 0.6$), as the galactic outflows are 3–4 times stronger in `CRMHD` (F. Rodríguez Montero et al. 2024, see their Figure 9). Furthermore, while galactic outflows of the order of a few $M_\odot\,\mathrm{yr}^{-1}$ are present at $0.2\,R_\mathrm{vir}$ in the `MHD` run, B/R is close to 1 because these outflows are mostly ionized and optically thin. In fact, the presence of blue-dominated spectra, even when galactic outflows are present, is not uncommon in other simulations (A. Smith et al. 2019, 2022; P. D. Mitchell et al. 2021; J. Blaizot et al. 2023).

The differences become more obvious when individual Lyα features are compared. Figure 5(a) shows the location of the red peak in velocity space (v_red) and the flux ratio (B/R) from the angle-averaged spectrum of each galaxy at $2 < z < 4$. Empty symbols correspond to the measurements without intergalactic medium (IGM) attenuation, while the filled symbols show the results after applying the simple IGM model of A. K. Inoue et al. (2014). The `CRMHD` sample shows larger v_red and lower B/R than `MHD`, which is indicative of strong outflows. Additionally, the entire `CRMHD` sample has red peak-dominant spectra ($B/R < 1$) even without IGM attenuation, while 37% of the `MHD` sample has $B/R > 1$. The fraction having $B/R > 1$ drops to 10% when IGM attenuation is included. More importantly, some of the `CRMHD` data exhibit v_red up to $\approx 400\,\mathrm{km\,s^{-1}}$, thus covering the wide range of v_red obtained from $z \sim 3$ LAEs (D. K. Erb et al. 2014) or low-z LAEs taken from the Lyman Alpha Spectral Database (LASD; A. Runnholm et al. 2021, references therein). In contrast, the `MHD` samples show v_red of up to $\approx 270\,\mathrm{km\,s^{-1}}$, which is significantly less than that shown by `CRMHD`, as dust effectively destroys Lyα photons before they diffuse in frequency. Taken at face value, the simulation with CR feedback (`CRMHD`) appears to predict Lyα properties that are more consistent with the LAE observations, while the simulation with the overcooling features (`MHD`) can only explain a limited range of galaxies on the v_red-B/R plane.

However, we find that more accurate ionization structures make the interpretation nontrivial. Figure 5(b) shows the Lyα properties obtained from the angle-averaged spectra after LyC postprocessing with RAMSES-RT. The mean v_red in the `CRMHD` run is remarkably reduced from $234\,\mathrm{km\,s^{-1}}$ (left panel) to $162\,\mathrm{km\,s^{-1}}$ (right panel), while the mean IGM-attenuated B/R increases from 0.29 to 0.61. Similarly, the `MHD` run shows a decrease in v_red and an increase in B/R, but the changes are less dramatic ($170 \rightarrow 153\,\mathrm{km\,s^{-1}}$, $0.61 \rightarrow 0.69$). As a result, the two different simulations predict similar Lyα line features overall, in contrast to the comparison of the simulations before postprocessing with RAMSES-RT. The similar B/R values can be partly attributed to IGM absorption, which suppresses the blue flux more strongly in the `MHD` sample.

To understand why v_red is significantly reduced in the `CRMHD` run, we examine a snapshot at $z = 2.7$, in which the galaxy exhibits the largest v_red ($\approx 400\,\mathrm{km\,s^{-1}}$), but a smaller v_red of $\approx 170\,\mathrm{km\,s^{-1}}$ after postprocessing. This galaxy undergoes a minor burst phase with a star formation rate of $3\,M_\odot\,\mathrm{yr}^{-1}$; however, it is not associated with mergers. The effective H I column densities ($N_\mathrm{HI,eff}$) measured from the LyC escape fraction are very similar before ($1.6 \times 10^{18}\,\mathrm{cm^{-2}}$) and after postprocessing ($9.8 \times 10^{17}\,\mathrm{cm^{-2}}$), but the Ly$\alpha$ escape fraction increases by an order of magnitude (1.1% versus 10.3%). Here, we use $N_\mathrm{HI,eff} = -\log_{10} f_\mathrm{LyC}^\mathrm{noDust}/\sigma_\mathrm{LyC}$, where $f_\mathrm{LyC}^\mathrm{noDust}$ is the luminosity-weighted escape fraction of the LyC photons, measured from each star particle within the virial sphere in the absence of dust, and $\sigma_\mathrm{LyC} = 6.3 \times 10^{-18}\,\mathrm{cm^{-2}}$ is the absorption cross-section at the Lyman edge. As we assume that LyC and Lyα photons are produced at the same positions, the marked difference demonstrates that Lyα is very efficient in finding and propagating along low-density channels, thus making it less sensitive to the mean optical depth of the volume-filling gas inside the virial sphere. Figure 3 supports this interpretation by showing that the fraction of sightlines with $N_\mathrm{HI} \leqslant 10^{18}\,\mathrm{cm^{-2}}$ increases from $\leqslant 0.1\%$ to only $\sim 1\%$ (before and after LyC postprocessing), but this change is sufficient to alter the Lyα profiles.

Lyα is highly sensitive to the geometry and velocity structures of the scattering medium, leading to significant variations in spectra along different sightlines compared with angle-averaged spectra (e.g., J. Blaizot et al. 2023). The effect of orientation can be seen in Figure 5(c), which shows the line properties computed from the IGM-attenuated, 1D mock spectra. To make a fair comparison with existing observed profiles, such as those from the Hubble Space Telescope Cosmic Origins Spectrograph, we include a collisional term and collect Lyα within a 2.″5 aperture.[9] For both simulations the distributions of v_red and B/R along the various sightlines

---

[9] We confirm that collecting Lyα within the entire virial radius does not significantly affect B/R. However, the number of sightlines showing large v_red ($\gtrsim 300\,\mathrm{km\,s^{-1}}$) increases notably in `MHD` ($7 \rightarrow 24$), as the contribution from Lyα photons with smaller velocity shifts in the outer halo is excluded (see, e.g., Y. Guo et al. 2024).

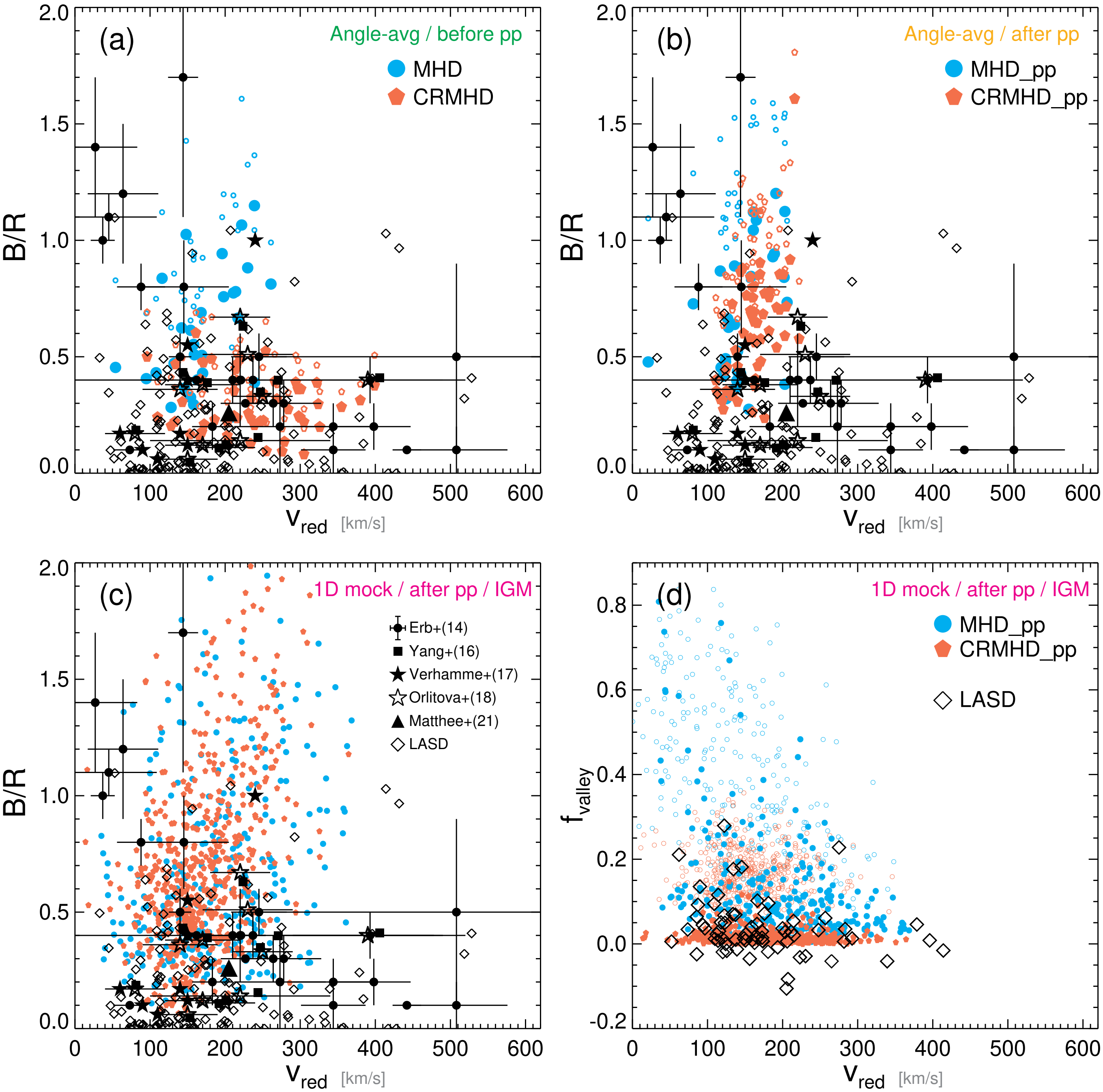

Figure 5. Comparison of the blue-to-red flux ratio of Lyα (B/R) and the location of the red peak ($v_{\rm red}$) in velocity space in simulations with (`CRMHD`) and without CRs (`MHD`). The upper panels show the angle-averaged quantities before (a) and after (b) LyC postprocessing with RAMSES-RT. The filled and empty symbols represent measurements after and without applying the simple IGM attenuation model of A. K. Inoue et al. (2014), respectively. Lyα properties estimated from 1D mock spectra within a $2\overset{''}{.}5$ aperture are compared in (c). The black symbols correspond to observational data from D. K. Erb et al. (2014), H. Yang et al. (2016), A. Verhamme et al. (2017), I. Orlitová et al. (2018), J. Matthee et al. (2021), A. Runnholm et al. (2021). Panel (d) shows the simulated ratio between the flux in the valley of the two peaks and the maximum of the peaks ($f_{\rm valley}$, filled circles). The black diamonds indicate the LASD values obtained using the systematic redshift. For comparison, we also include $f_{\rm valley}$ values, calculated using Lyα collected within the entire virial sphere (empty circles).

are broader, with $B/R \lesssim 2$ and $v_{\rm red} \lesssim 350\,{\rm km\,s^{-1}}$, in contrast with the angle-averaged values. The remarkable similarity in $v_{\rm red}$ and B/R distributions predicted by the two simulations, with and without CR-driven winds, suggests that these two metrics might not be enough to distinguish different feedback models, unless very large observational samples are available.

Nevertheless, the comparison with observations provides some useful insights into gas kinematics. The `CRMHD` galaxy shows a median $v_{\rm red}$ of $151\,{\rm km\,s^{-1}}$, comparable to that of the local (H. Yang et al. 2016; A. Verhamme et al. 2017; I. Orlitová et al. 2018; A. Runnholm et al. 2021) or high-z LAEs (D. K. Erb et al. 2014). The IGM-attenuated B/R (0.64, median) is also broadly consistent with the observations, but tends to be higher than the average value of the D. K. Erb et al. (2014) sample (0.4) or local LAE values of ≈0.1 (A. Runnholm et al. 2021). Without the IGM attenuation, the simulated B/R increases to ≈1.0. Moreover, a significant fraction (21%) of the simulated profiles with IGM attenuation are blue-dominated ($B/R > 1$), while the fraction appears lower (∼13%) in a sample of 32 LAEs at $z \sim 2.7$ (R. F. Trainor et al. 2015). Although these blue-dominated galaxies could possibly represent quiescent phases and are thus more difficult to observe (J. Blaizot et al. 2023), the overprediction of B/R indicates that both simulations may be lacking outflows. The paucity of galaxies with large $v_{\rm red}$ ($\gtrsim 350\,{\rm km\,s^{-1}}$) is likely a related problem, although it is equally possible that the large $v_{\rm red}$ values in the observations arise simply because the observed samples are brighter than the simulated ones, as discussed further in Section 4.1.

3.2.2. Valley Flux

M. Gronke et al. (2018) showed that the impact of CR-driven winds is more evident when comparing the flux ratio ($f_{\rm valley}$) between the valley ($F_{\rm valley}$) and maximum ($F_{\rm max}$) of the two peaks. Their ISM simulations without CRs produce Lyα spectra with a high value of $0.3 \lesssim f_{\rm valley} \lesssim 0.7$, while $f_{\rm valley}$ in their CR simulations can be as small as ∼0.1 owing to the suppression of Lyα escape at the line center by the extended neutral outflows. We also measure the flux ratio from 1D mock spectra extracted within a 2.″5 aperture and compare it with the recent LASD data from A. Runnholm et al. (2021) in Figure 5(d). Because measuring the valley flux requires a high spectral resolution and can therefore be uncertain depending on the instrument used, we include only those samples for which $F_{\rm valley}$ measurements from two independent redshift determination methods are available and agree within $\Delta F_{\rm valley} < 0.2$ for conservative estimates.

We find that simulations without CRs predict a mean valley flux ratio of $\langle f_{\rm valley} \rangle = 0.12 \pm 0.13$, while $f_{\rm valley}$ values are further reduced in the presence of CR-driven winds (0.02 ± 0.02), where the range represents the standard deviation. The sightlines from the `CRMHD` run show greater overlap with the observed distribution of $\langle f_{\rm valley} \rangle \approx 0.04 \pm 0.07$, while a non-negligible fraction of the `MHD` run exhibits large $f_{\rm valley}$ values of $\gtrsim 0.2$. However, both simulations yield results that are broadly consistent with observations. This level of agreement is somewhat unexpected, particularly in the `MHD` run, considering that its angle-averaged profile shows a prominent flux at the line center in Figure 4.

To illustrate the importance of aperture effects in interpreting the Lyα profiles, we remeasure $f_{\rm valley}$ by collecting Lyα within the entire virial sphere (shown as empty circles in Figure 5, panel (d)). In contrast to $f_{\rm valley}$ measured within the central ∼10 kpc radius (i.e., 2.″5 diameter), the flux at line center in the `MHD` run becomes much more prominent ($\langle f_{\rm valley} \rangle = 0.40 \pm 0.19$), indicating that Ly$\alpha$ from the outer halo contributes preferentially near line center (e.g., D. K. Erb et al. 2023; Y. Guo et al. 2024). The $f_{\rm valley}$ values within the virial sphere from the `CRMHD` run are also increased to $\langle f_{\rm valley} \rangle = 0.17 \pm 0.06$, but they remain significantly lower than those in `MHD`. This difference can be attributed to the fact that, in the `MHD` simulation, ≈97% of the Lyα photons are destroyed by dust owing to high column densities, thus making the emergent signal more sensitive to photons originating in low-density regions. By directly comparing the emergent line profiles between `MHD` and `CRMHD` runs, we confirm that the valley flux is not necessarily high in the `MHD` run, but the flux at reasonably large velocity shifts, and thus $F_{\rm max}$, is significantly suppressed.

Our findings support the conclusion that CR-driven winds can lead to lower $f_{\rm valley}$ values (see M. Gronke et al. 2018, for ISM patch simulations). However, low $f_{\rm valley}$ can also result from a small observational aperture, which preferentially captures photons that undergo multiple scatterings through an optically thick ISM. In this context, the behavior of $f_{\rm valley}$ measured over larger spatial scales may be more useful, as it may reflect the angle-averaged properties of the Lyα spectra better, thereby motivating further investigation.

3.3. Lyα Surface Brightness Profiles

The previous section showed that the presence of ionized channels allows efficient escape of Lyα. These escaped photons will subsequently scatter with the neutral H I in the CGM. An enhanced H I spatial distribution, resulting from CR feedback, could enhance this scattering and potentially leave an imprint on the surface SB profiles. To investigate this possibility, we median-stack the SB profiles obtained along 10 different sightlines per snapshot and combine the results for two different redshift ranges $2 \leqslant z \leqslant 3$ and $3 \leqslant z \leqslant 4$. Following P. D. Mitchell et al. (2021), the SB profiles are point-spread function (PSF)-convolved using a Moffat function with $\beta = 2.8$ and ${\rm FWHM}/'' = 0.875 - (\lambda/10^4\,{\rm Å})/3$. To correct for the redshift dimming effect, we multiply the brightness by $(1+z)^4$ and assume that all the samples are placed at $z = 3$. Again we use the simulation data, postprocessed with ionizing radiative transfer for both `CRMHD` and `MHD` runs, and include the contribution from collisional radiation. The intrinsic Lyα luminosity from collisional radiation in the `CRMHD` run is, on average, ∼3 times brighter than that in `MHD`, but it accounts for only ≈15% of the total Lyα.

Figure 6 (lower panel) shows that Lyα emission is more extended in the CR feedback run for a given observation threshold. As aforementioned, although the intrinsic Lyα luminosity of the `CRMHD` sample is half as bright as that of `MHD`, Lyα escapes more efficiently. As a result, the attenuated luminosities are, on average, 1.9 times brighter in `CRMHD` than in `MHD`. This is evident when comparing the colored solid lines, where the thin lines indicate the PSF-smoothed total intrinsic SB profiles (including collisional radiation), while the thick lines denote the PSF-smoothed emergent profiles at $3 < z < 4$. In particular, the emergent SB profile from the `CRMHD` run at $r > 20$ kpc is brighter than the intrinsic profile, clearly indicating that scattering with the neutral CGM facilitates more extended Lyα emission. Interestingly, in the case of the `MHD` run, the inefficient escape of Lyα is seen not only in the central region, but also in the outer halo. This is due to the fact that satellite galaxies in the `MHD` run are overcooled and contribute a significant fraction of intrinsic radiation even at $10 \lesssim r \lesssim 30$ kpc.

It is also interesting to compare Lyα profiles originating from collisional radiation. Because cooling radiation is produced in more extended regions, it escapes more easily ($f_{\rm Ly\alpha,coll} \sim 0.5$) than that from young stars and is therefore more affected by the CGM. For example, the effective radius of the intrinsic cooling radiation in `CRMHD` is three times larger (7 kpc before PSF smoothing) than that of the young stars (2.3 kpc). Although not shown, we find again that at $r \gtrsim 20$ kpc, the emergent cooling radiation in the `CRMHD` run becomes brighter than the intrinsic emission, while the emergent SB profile in `MHD` remains fainter than its intrinsic

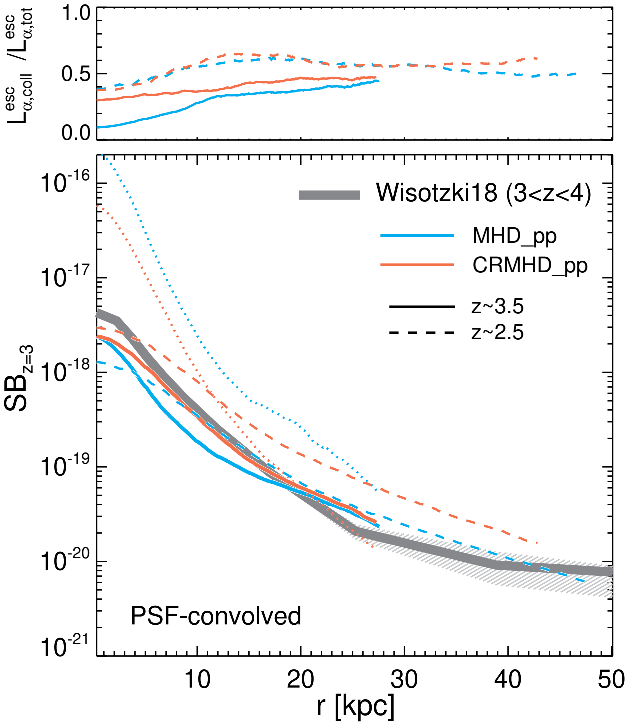

Figure 6. Upper panel: fractions of collisional radiation to the total emergent, PSF-convolved Lyα SB profiles. Solid and dashed lines show results for different redshift ranges ($2 < z < 2.5$ and $3 < z < 3.5$, respectively). Lower panel: median-stacked SB profiles of galaxies simulated without (`MHD`, cyan) and with (`CRMHD`, orange) CR feedback. The median-stacked SB profile of LAEs at $z \sim 3.5$, obtained with the MUSE instrument, is included for comparison (thick gray line with shaded regions, L. Wisotzki et al. 2018). We also include the PSF-smoothed intrinsic SB profiles as dotted lines. To correct for the redshift dimming effect, the SB profiles are scaled by a factor of $(1 + z)^4/(1 + 3)^4$.

profile at all radii; this supports our interpretation of the impact of CR driven outflows on the extended Lyα SB profile.

The SB profiles simulated with CR feedback are in good agreement with those of the observed LAEs. The gray thick line in Figure 6 illustrates the median-stacked SB profile of 92 LAEs obtained with MUSE at $3 < z < 4$ (L. Wisotzki et al. 2018). Note that the MUSE sample has UV magnitudes comparable to those of the `CRMHD` galaxies in the same redshift range. Our simulations at $z \sim 3.5$ predict Lyα profiles that closely match the observations, although the SB from the `MHD` run is slightly fainter. As expected, the simulations at lower redshifts ($z \sim 2.5$) yield brighter profiles than their $z \sim 3.5$ progenitors, as star formation becomes more active in more massive galaxies. The more luminous LAE subsample in L. Wisotzki et al. (2018) with $>10^{42}\,\mathrm{erg\,s^{-1}}$ indeed shows systemically brighter SB profiles (see also H. Kusakabe et al. 2022).

Using a cosmological radiation-hydrodynamic simulation of a dark matter halo of mass $10^{11}\,M_\odot$ at $z = 3$, P. D. Mitchell et al. (2021) successfully reproduce the SB profile of L. Wisotzki et al. (2018) and argue that collisional excitation alone accounts for half of the SB in the CGM region ($r \gtrsim 10$ kpc). Figure 6 (upper panel) shows that in our simulations, both with and without CR pressure, collisional radiation also explains ∼30%–50% of the total Lyα SB in the CGM region (see also A. Smith et al. 2019). However, our simulations reveal additional complexity in accounting for the remaining SB. In the `CRMHD` run, the CR-driven outflows shape the extended Lyα halo by reducing the surrounding gas density near the young stars. This, in turn, facilitates the escape of more photons and scattering in the CGM, resulting in a more extended Lyα halo. In contrast, in the over-cooled `MHD` galaxy, a large amount of Lyα is produced and destroyed, with only a small fraction reaching the CGM. Although CR feedback is not included in P. D. Mitchell et al. (2021), enhanced Lyα escape is achieved via boosted SN feedback. Based on the results from the IllustrisTNG simulations (A. Pillepich et al. 2018; D. Nelson et al. 2019), C. Byrohl et al. (2021) show that the SB profiles from F. Leclercq et al. (2017) can be reproduced if dust is absent in low-mass galaxies. All of these possibilities suggest that no unique mechanism exists for generating extended Lyα SB, and multiple scenarios must be explored in parallel to constrain galaxy formation models using SB observations.

4. Discussion

4.1. Lack of Lyα Line Profiles with Strong Outflow Features

The previous section showed that a majority of galaxies postprocessed with RAMSES-RT have Lyα features consistent with those of local star-forming galaxies (e.g., H. Yang et al. 2016; A. Verhamme et al. 2017; I. Orlitová et al. 2018). However, only a few simulated samples have a Lyα profile with both a large $v_{\rm red}$ of $\gtrsim 350\,\mathrm{km\,s^{-1}}$ and a low B/R of $\lesssim 0.5$. These combined features can be interpreted as indicative of strong neutral outflows (e.g., M. Dijkstra et al. 2006; A. Verhamme et al. 2006), thus motivating further discussion of the comparison between simulations and observations.

To understand the origin of a large $v_{\rm red}$, we first focus on the `CRMHD` galaxies that show $v_{\rm red} \sim 400\,\mathrm{km\,s^{-1}}$ in the spectra computed without LyC postprocessing (see panel (a) in Figure 5). To determine whether the ISM or CGM is primarily responsible for shaping the Lyα profile, we perform MC Lyα RT twice, once without the ISM and once without the CGM. For simplicity, collisional radiation is neglected in this exercise. Separating the ISM from the CGM is nontrivial, and we simply assume that the gas within $0.1\,R_{\rm vir}$ (≈ 5 kpc) is more associated with the ISM. This is motivated by the fact that R_{90} is ≈ 4.5 kpc at this redshift, where R_{90} is the radius within which 90% of the UV light is confined. Note that the Lyα source positions are taken from stellar positions within $r < 0.1\,R_{\rm vir}$ and thus differ slightly from the source positions used in Figure 5, where all the stellar particles within $r < R_{\rm vir}$ are used along with collisional radiation. In the case of the sightline with the largest $v_{\rm red}$ of $400\,\mathrm{km\,s^{-1}}$, only ∼1% of the Lyα photons escape their virial halo and show $v_{\rm red}$ of $\sim 250\,\mathrm{km\,s^{-1}}$ when Lyα photons interact only at $r < 0.1\,R_{\rm vir}$.[10] Conversely, if the scattering occurs only in the outer region ($r > 0.1\,R_{\rm vir}$), ∼97% of them leave the halo with $v_{\rm red} \sim 150\,\mathrm{km\,s^{-1}}$. In the latter case, the spectrum is dominated by the blue peak ($B/R = 1.6$ without IGM attenuation), indicating that a significant fraction of the neutral gas is collapsing in the outer region (Y. Guo et al. 2024; Y. Yuan et al. 2024). Indeed, we confirm that the volume-filling neutral hydrogen in this simulated galaxy tends to be inflowing rather than outflowing.

---

[10] Unlike the other cases, this particular snapshot has a strong Lyα emission from satellites, which complicates the interpretation of the profile in terms of $N_{\rm HI}$; however, the ISM region still plays a more important role than the CGM in setting the large $v_{\rm red}$.

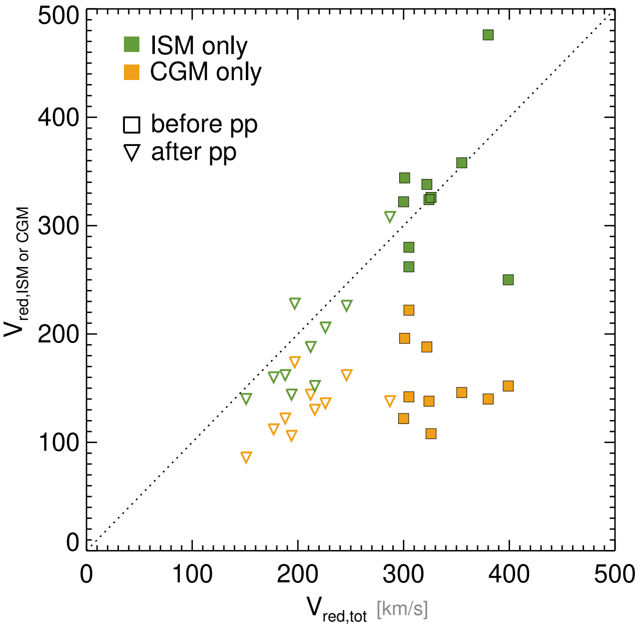

Figure 7. Predicted Lyα profiles formed by ISM region ($r < 0.1\,R_{\rm vir}$, green symbols) or by CGM ($r > 0.1\,R_{\rm vir}$, orange symbols). Note that the source positions are limited to $r < 0.1\,R_{\rm vir}$ for $v_{\rm red,ISM}$ or $v_{\rm red,CGM}$ for easier interpretation. The $v_{\rm red,tot}$ values are the same as the $v_{\rm red}$ values in Figure 5 (left panel) and thus are obtained from all the photons generated within the virial sphere. The location of the red peak from the galaxy ($v_{\rm red}$) is compared before (squares) and after (triangles) LyC postprocessing with RAMSES-RT.

To be more quantitative, we repeat this exercise for all snapshots showing $v_{\rm red} \geqslant 300\,{\rm km\,s^{-1}}$ in their angle-averaged spectrum in the `CRMHD` run before LyC postprocessing. Figure 7 (filled symbols) shows that although the CGM alone can produce $v_{\rm red}$ of 100–200 ${\rm km\,s^{-1}}$, the peak location is primarily determined by the gas within $0.1\,R_{\rm vir}$. If the scattering medium were uniform with a fixed temperature of 10^4 K (Equation (1)), the $v_{\rm red}$ values inside and outside $0.1\,R_{\rm vir}$ would imply that the scattering $N_{\rm HI}$ in the inner region is an order of magnitude larger than that of the CGM ($\sim 6 \times 10^{20}$ versus $7 \times 10^{19}\,{\rm cm^{-2}}$). Ly$\alpha$ processed by the inner gas often has larger $v_{\rm red}$ values compared with those influenced by the ISM and CGM together ($v_{\rm red}$ in the left panel of Figure 5). However, this difference is simply due to the different source positions within $0.1\,R_{\rm vir}$, as shown in Figure 7, which was intended to minimize the complexity of the source geometry due to satellites.

The contribution of the inner gas to $v_{\rm red}$ in the `CRMHD` run decreases when more precise ionization structures are used (open symbols), but it remains the dominant component shaping the line profile compared with the CGM. Comparing the relative shift between the filled and empty symbols in Figure 7, the decrease in $v_{\rm red}$ can be attributed to the change in the ionization structures of the inner halo rather than that of the CGM. We recall that $N_{\rm HI}$ around young stellar populations does not vary significantly before and after the LyC postprocessing, suggesting that this subtle change in the ionized structure of the ISM region leads to the significant decrease in $v_{\rm red}$. In fact, the analytical calculation (Equation (1)) suggests that $N_{\rm HI}$ needs to be of the order of $10^{21}\,{\rm cm^{-2}}$ to accommodate the large $v_{\rm red}$ of $\gtrsim$400–500 ${\rm km\,s^{-1}}$, but the actual $v_{\rm red}$ is significantly smaller even though the column density distributions in our simulations peak around $N_{\rm HI} \sim 10^{22}\,{\rm cm^{-2}}$ (Figure 3) (see also M. Gronke & M. Dijkstra 2016).

High-resolution galactic-scale simulations show that the ISM is highly turbulent and mostly supported by warm structures owing to the self-regulation of star formation processes (e.g., P. Hennebelle & O. Iffrig 2014; A. Gatto et al. 2017; C.-G. Kim & E. C. Ostriker 2018, to name a few). Such turbulent structures seem to be missing in the simulations presented here. This may be due to finite resolution, the absence of radiation feedback (J. Rosdahl et al. 2015; M. Y. Grudić et al. 2018; J.-G. Kim et al. 2018), a simple chemical network (H. Katz et al. 2022; J.-G. Kim et al. 2023), or an inefficient star formation model (O. Agertz & A. V. Kravtsov 2015; C. Kang et al. 2025). For example, when star formation is efficient (locally), radiation feedback can disrupt GMCs within several Myr via photoionization heating (e.g., T. Kimm et al. 2022). Direct radiation pressure can also contribute in dense regions ($n_{\rm H} \gtrsim 10^5\,{\rm cm^{-3}}$, T. Kimm et al. 2017), but it is less significant than photo-ionization heating (e.g., J.-G. Kim et al. 2018). Although stellar radiation feedback alone cannot drive strong galactic winds, subsequent SN explosion energy can escape freely from their natal clouds, providing support against gravitational collapse (F. Bournaud et al. 2010; E. C. Ostriker et al. 2010) and driving galactic turbulence in a multiphase ISM (M. K. R. Joung & M.-M. Mac Low 2006; P. Padoan et al. 2016). Because even a small fraction of sightlines with low $N_{\rm HI}$ can significantly reduce the Lyα line width, the development of the multiphase ISM would help Lyα photons escape more freely, thereby further reducing the number of scatterings with dusty cold ISM and increasing $L_{\rm Ly\alpha}$. On the other hand, heating the cold dense phase into the volume-filling warm neutral phase by effective stellar feedback could populate relatively high $N_{\rm HI}$ lines of sight with little dust, potentially enhancing $v_{\rm red}$. Thus, further investigations are needed to determine whether the structural properties of the warm ISM actually facilitate enhanced Lyα scattering. An example based on the TIGRESS ISM model (C.-G. Kim & E. C. Ostriker 2018) shows the angle-averaged Lyα spectra with $v_{\rm red} \sim 200\,{\rm km\,s^{-1}}$ (K.-i. Seon & C.-G. Kim 2020), which may not be sufficient to explain the observed $v_{\rm red}$, even though galactic outflows extending into the CGM could potentially lead to higher $v_{\rm red}$ values.

Another missing component of simulated galaxies is the multiphase structure of the diffuse, low-density CGM. Increased resolution in the CGM helps to better resolve thermally unstable gas and hydrodynamic instabilities, leading to the development of more cool structures (C. B. Hummels et al. 2019; M. S. Peeples et al. 2019; J. Suresh et al. 2019; M. P. Rey et al. 2024). This, in turn, could enhance the cooling radiation in the CGM (e.g., Z. Haiman et al. 2000). A similar idea has been proposed by S. Cantalupo et al. (2014), who claim that substantial clumping is required to explain observations of giant Lyα nebulae. Considering that the stellar mass of the `CRMHD` galaxy lies slightly above the average stellar mass-to-halo mass relation (e.g., P. S. Behroozi et al. 2013), more efficient feedback may still be required, and cooling radiation may be enhanced owing to the increased gas content in the CGM. However, a highly structured CGM is unlikely to boost Lyα scattering, making the detection of galaxies with large $v_{\rm red}$ difficult.

Admittedly, direct comparisons between observations and simulations should be made with caution. Some observed samples with large $v_{\rm red}$ are detected with low signal-to-noise ratio at finite spectral resolution, and the precise determination of $v_{\rm red}$ and B/R faces uncertainties, as indicated by the large errors in Figure 5. Additionally, we simulated only one galaxy, whereas observational data likely correspond to different phases of galaxy evolution (see J. Blaizot et al. 2023 for an example that recovers diverse Lyα profiles using a single galaxy). Increasing the number of mock spectra could also help explain rare features, as the dependence of line properties on sightline variations can be significant (J. Blaizot et al. 2023; Y. Yuan et al. 2024). Indeed, although the angle-averaged $v_{\rm red}$ is small ($\lesssim$250 km s^{-1}), the `CRMHD` run reveals a few cases with a large $v_{\rm red}$ of $\sim$350 km s^{-1} (Figure 5); however, the fraction of galaxies with such large $v_{\rm red}$ values appears too small to be consistent with observations. This may be partly because galaxies with large $v_{\rm red}$ in D. K. Erb et al. (2014) tend to be brighter ($-21 \lesssim M_{\rm UV} \lesssim -19$) than our simulated galaxies. R. F. Trainor et al. (2015), for example, report that galaxies with $v_{\rm red} \gtrsim 400$ km s^{-1} are more commonly observed at $M_{\rm UV} \lesssim -20$. Therefore, future studies are needed to simulate a brighter sample to make a more rigorous comparison and draw a firm conclusion on the paucity of galaxies with large $v_{\rm red}$.

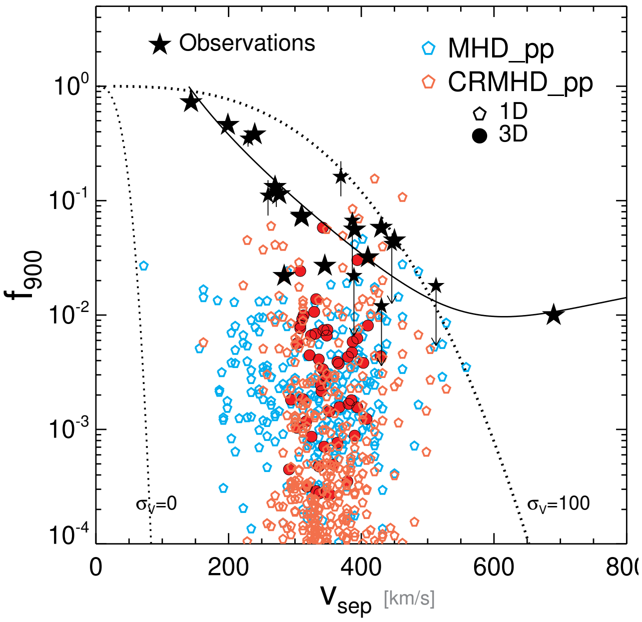

Figure 8. Correlation between separation of double peaks in Lyα ($v_{\rm sep}$) and escape fraction at 900 Å (f_{900}). The black star symbols represent the observed properties of LAE galaxies from A. Verhamme et al. (2017), while the colored points denote the results from simulations (empty: 1D, filled: 3D). The black solid line is the empirical relation from Y. I. Izotov et al. (2018c). For comparison, we include the analytic correlation between $v_{\rm sep}$ and f_{900} for dust-free uniform media with turbulence velocities of 0 and 100 km s^{-1} (dotted lines). No clear correlation is found between f_{900} and $v_{\rm sep}$ at $f_{900} \lesssim 0.1$.

4.2. Implications of the Sensitive Behavior of Lyα

Using two idealized configurations of homogeneous or clumpy spherical shells, A. Verhamme et al. (2015, 2017) suggested that the separation of the blue and red peaks ($v_{\rm sep}$) could be used to select the LyC leakers. The idea is that galaxies with low-density channels that allow LyC photons to escape would experience fewer scatterings, resulting in a low $v_{\rm sep}$ of $\lesssim$300 km s^{-1}. Based on the Cosmic Origin Spectrograph data of five local LyC leakers and results from the literature, Y. I. Izotov et al. (2018a, 2018c) further argue for a tight correlation between $v_{\rm sep}$ and the LyC escape fraction (see also S. R. Flury et al. 2022; R. P. Naidu et al. 2022), thus supporting the claim by A. Verhamme et al. (2015).

In Figure 8, we compare $v_{\rm sep}$ with the LyC escape fraction at 900 Å (f_{900}). Observational data from A. Verhamme et al. (2017), Y. I. Izotov et al. (2018a, 2018b, 2021) are shown as star symbols, along with an empirical relation by Y. I. Izotov et al. (2018c). Orange empty hexagons correspond to measurements along different sightlines in the `CRMHD` run at different redshifts, while cyan hexagons represent measurements from the `MHD` run. As already shown in Figure 5, the two simulation sets do not exhibit a clear difference in $v_{\rm sep}$. However, the `CRMHD` sample tends to display lower f_{900} than does the `MHD` run, as the volume-filling, extended H I in the CR run absorbs LyC radiation more efficiently (see M. Farcy et al. 2025, for results from cosmological simulations). Nevertheless, distinguishing between the two models in the $v_{\rm sep}$-f_{900} plane remains nontrivial owing to the significant overlap.

Our results further suggest that the $v_{\rm sep}$–f_{900} correlation is likely weak among non-LyC leakers, regardless of the model assumptions. Although some simulated samples overlap with the properties of local galaxies (e.g., A. Verhamme et al. 2017), virtually no correlation exists between $v_{\rm sep}$ and f_{900} at $f_{900} \lesssim 0.1$. This is true even when comparing angle-averaged quantities (red filled circles), suggesting that the highly sensitive nature of Lyα prevents one from inferring the escape fraction at these low f_{900} regimes. Using a large number of simulated galaxies at $z \gtrsim 5$, N. Choustikov et al. (2024) also reach the same conclusion, while the majority of LyC leakers still exhibit $v_{\rm sep} \lesssim 300$ km s^{-1}. The considerable scatter found at $f_{900} \lesssim 0.1$ in recent observations (S. R. Flury et al. 2022; R. P. Naidu et al. 2022) also appears consistent with our interpretation.

Another intriguing question is whether the Lyα peak location can be used to trace the outflow velocity of the neutral medium. Using a shell model, M. Gronke et al. (2015) demonstrate that the two most important parameters, $N_{\rm HI}$ and outflow velocity, can be reasonably recovered by fitting the Lyα profiles. However, extracting the information becomes progressively difficult when the medium is highly clumpy (e.g., M. Gronke & M. Dijkstra 2016). Our results also support this, showing that the presence of low-density channels can significantly alter the emergent Lyα spectra. Moreover, sightline-to-sightline variations in Lyα profiles are substantial. A recent study by Y. Yuan et al. (2024) also showed that $v_{\rm sep}$ is not strongly correlated with H I-weighted velocity, although sightlines with low B/R generally trace outflows. Indeed, analyzing the UV and Lyα spectra of local star-forming galaxies from the Lyman Alpha Reference Sample, T. E. Rivera-Thorsen et al. (2015) find little correlation between $v_{\rm red}$ and the outflow velocity inferred from other low-ionization metal absorption lines. Given these complexities, extracting physical properties from individual spectra may be challenging. Instead, simultaneously reproducing SB profiles and Lyα line features for a statistical sample may be more useful to infer general kinematic properties of the neutral medium and constrain feedback models in simulations (e.g., H. Song et al. 2020).

5. Summary and Conclusions

This study investigated the impact of CR feedback on the Lyα emission properties of a simulated galaxy embedded in a $10^{11}\,M_\odot$ dark matter halo at $z = 2$. To this end, we used cosmological MHD simulations with (`CRMHD`) and without CRs (`MHD`) (F. Rodríguez Montero et al. 2024) and postprocessed them with ionizing radiation transfer using RAMSES-RT to obtain more accurate hydrogen ionization structures. We then performed Monte Carlo Lyα radiative transfer with RASCAS (L. Michel-Dansac et al. 2020) and measured several line properties: the relative peak strength (B/R), location of the red peak ($v_{\rm red}$), and relative flux ratio between the valley and the maximum of the two peaks ($f_{\rm valley}$). The comparison of simulated Lyα with and without CRs, together with the observed Lyα features of LAEs, revealed the following key features.

1. The simulation with CR-driven outflows reasonably reproduces the UV and Lyα luminosities of observed LAEs. In contrast, the simulation without CRs predicts galaxies that are fainter in Lyα for a given M_{1500}, compared with the observations. (Figure 2). Although galaxies simulated with CRs form fewer stars by a factor two, their attenuated Lyα luminosities are two times brighter, as Lyα escapes more efficiently owing to a lower $N_{\rm HI}$ distribution (Figure 3).
2. Despite the significant difference in $N_{\rm HI}$, the resulting $v_{\rm red}$ computed from angle-averaged line profiles is very similar between the `CRMHD` and `MHD` runs (Figure 5(b)). Optically thick, dusty galaxies from the `MHD` run predict an intermediate $v_{\rm red}$ of 100–200 km s^{-1} (angle-averaged), as dust preferentially destroys Lyα photons that undergo a large number of scatterings. On the other hand, the `CRMHD` galaxy shows similar $v_{\rm red}$ values because Lyα photons propagate preferentially along low $N_{\rm HI}$ channels. Orientation effects further increase the scatter (Figure 5(c)). Both simulations predict values of $v_{\rm sep} \sim 160$ km s^{-1} and $B/R \sim 0.7$ in the mock spectra, which are broadly consistent with existing observations, although the average B/R values tend to be higher than the observed ones.
3. The simulations postprocessed with LyC radiative transfer do not produce galaxies with $v_{\rm red} \gtrsim 350$ km s^{-1} and $B/R < 0.5$. However, when the neutral hydrogen fraction is assumed to be determined by collisional equilibrium and fills the optically thin channels near young stars, the galaxies affected by CRs yield large angle-averaged $v_{\rm red}$ values of up to 400 km s^{-1} (Figure 5(a)). This simple experiment suggests that galaxies with large $v_{\rm red}$ may be better explained if more volume-filling neutral hydrogen is present within the inner virial sphere (Figure 7).
4. The `CRMHD` run yields flux ratios between the valley and maximum of the two peaks $f_{\rm valley} = 0.02 \pm 0.02$, consistent with the low-z LSAD sample ($f_{\rm valley} = 0.04 \pm 0.07$). The over-cooled galaxy without CR predicts a slightly higher $f_{\rm valley} = 0.12 \pm 0.13$.
5. CR feedback produces more extended H I distributions in the CGM (Figure 1). The model reproduces the Lyα SB of faint LAEs observed with MUSE (L. Wisotzki et al. 2018) (Figure 6), while the over-cooled galaxy exhibits slightly fainter profiles. Our results also confirm previous findings that approximately half of the Lyα emission in the CGM region likely originates from collisional excitation, while the other half comes from recombinative radiation by young stars.
6. The LyC escape fraction (f_{900}) is predicted to be lower with CR feedback, due to the extended H I distribution, although the difference in f_{900} between the two simulations is not sufficiently significant to place strong constraints on the feedback models. For non-LyC leakers ($f_{900} \lesssim 0.1$), the peak separation of Lyα ($v_{\rm sep}$) shows little correlation with f_{900} (Figure 8).

While individual Lyα features, such as B/R or $v_{\rm red}$, may not directly constrain the galaxy formation models, the differences between the simulated and observed mean B/R suggest that current simulations still need to improve CR transport (e.g., P. F. Hopkins et al. 2021; A. Nuñez-Castiñeyra et al. 2022), resolution (e.g., M. S. Peeples et al. 2019; J. Suresh et al. 2019), and/or lack crucial baryonic processes, such as bursty star formation (e.g., C. Kang et al. 2025). Comparison of simulated Lyα features with statistically significant samples of LAEs remains valuable, offering an independent perspective. Furthermore, numerical modeling of Lyα emission at different scales is essential for interpreting statistical LAE data and leveraging these samples to constrain structure formation and cosmology. The sensitive nature of Lyα, rather than being a limitation, provides a unique opportunity for future astrophysical studies.

Acknowledgments

We thank Lutz Wisotzki for sharing their data with us and are also grateful to the referee for constructive comments. T.K. was supported by the National Research Foundation of Korea (RS-2022-NR070872 and RS-2025-00516961) and also by the Yonsei Fellowship, funded by Lee Youn Jae. H.S. acknowledges the support of the National Research Foundation of Korea (No. 2022R1A4A3031306), funded by the Korean government (MSIT). This work used the DiRAC Data Intensive service (DIaL2 / DIaL3) at the University of Leicester, managed by the University of Leicester Research Computing Service on behalf of the STFC DiRAC HPC Facility (www.dirac.ac.uk). The DiRAC service at Leicester was funded by BEIS, UKRI and STFC capital funding and STFC operations grants. DiRAC is part of the UKRI Digital Research Infrastructure. The supercomputing time for numerical experiments was kindly provided by KISTI (KSC-2024-CRE-0200), and large data transfer was supported by KREONET, which is managed and operated by KISTI.

Appendix
Postprocessing of Simulations

We postprocess the simulations with ionizing radiative transfer using RAMSES-RT to obtain more accurate estimates of neutral hydrogen. This is accomplished by running the simulations without updating the hydrogen densities but only changing the temperature and ionization fractions. We select three random snapshots and run RAMSES-RT for ~50 Myr, determining the timescale for the LyC escape fractions to converge to >98% (20 Myr). We then postprocess all the snapshots for 20 Myr before performing the Lyα radiative transfer. Figure A1 shows an example of the change in ionization structures after the LyC radiative transfer. Most of the neutral hydrogen remains nearly intact, while $N_{\rm HI}$ is notably reduced along some channels. On average, $N_{\rm HI}$ changes only to a small extent.

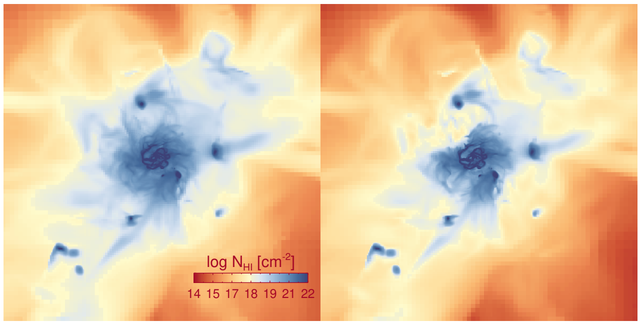

Figure A1. Example of $N_{\rm HI}$ map before (left) and after (right) the LyC postprocessing.

ORCID iDs

Taysun Kimm https://orcid.org/0000-0002-3950-3997
Julien Devriendt https://orcid.org/0000-0002-8140-0422
Jérémy Blaizot https://orcid.org/0000-0002-7534-8314
Harley Katz https://orcid.org/0000-0003-1561-3814
Beomchan Koh https://orcid.org/0009-0002-3737-8384
Hyunmi Song https://orcid.org/0000-0002-4362-4070

References

Agertz, O., & Kravtsov, A. V. 2015, ApJ, 804, 18
Agertz, O., Renaud, F., Feltzing, S., et al. 2021, MNRAS, 503, 5826
Behroozi, P. S., Wechsler, R. H., & Conroy, C. 2013, ApJ, 770, 57
Blaizot, J., Garel, T., Verhamme, A., et al. 2023, MNRAS, 523, 3749
Bournaud, F., Elmegreen, B. G., Teyssier, R., Block, D. L., & Puerari, I. 2010, MNRAS, 409, 1088
Byrohl, C., Nelson, D., Behrens, C., et al. 2021, MNRAS, 506, 5129
Calzetti, D., Kinney, A. L., & Storchi-Bergmann, T. 1994, ApJ, 429, 582
Cantalupo, S., Arrigoni-Battaia, F., Prochaska, J. X., Hennawi, J. F., & Madau, P. 2014, Natur, 506, 63
Caprioli, D., & Spitkovsky, A. 2014, ApJ, 783, 91
Chan, T. K., Kereš, D., Hopkins, P. F., et al. 2019, MNRAS, 488, 3716
Choustikov, N., Katz, H., Saxena, A., et al. 2024, MNRAS, 532, 2463
Dashyan, G., & Dubois, Y. 2020, A&A, 638, A123
Davé, R., Anglés-Alcázar, D., Narayanan, D., et al. 2019, MNRAS, 486, 2827
DeFelippis, D., Bournaud, F., Bouché, N., et al. 2024, MNRAS, 530, 52
Dijkstra, M. 2014, PASA, 31, e040
Dijkstra, M., Haiman, Z., & Spaans, M. 2006, ApJ, 649, 14
Dubois, Y., Beckmann, R., Bournaud, F., et al. 2021, A&A, 651, A109
Dubois, Y., Commerçon, B., Marcowith, A., & Brahimi, L. 2019, A&A, 631, A121
Erb, D. K., Li, Z., Steidel, C. C., et al. 2023, ApJ, 953, 118
Erb, D. K., Steidel, C. C., Trainor, R. F., et al. 2014, ApJ, 795, 33
Farcy, M., Rosdahl, J., Dubois, Y., Blaizot, J., & Martin-Alvarez, S. 2022, MNRAS, 513, 5000
Farcy, M., Rosdahl, J., Dubois, Y., et al. 2025, A&A, 698, A89
Flury, S. R., Jaskot, A. E., Ferguson, H. C., et al. 2022, ApJ, 930, 126
Fromang, S., Hennebelle, P., & Teyssier, R. 2006, A&A, 457, 371
Garel, T., Michel-Dansac, L., Verhamme, A., et al. 2024, A&A, 691, A213
Gatto, A., Walch, S., Naab, T., et al. 2017, MNRAS, 466, 1903
Gawiser, E., Francke, H., Lai, K., et al. 2007, ApJ, 671, 278
Geen, S., Rosdahl, J., Blaizot, J., Devriendt, J., & Slyz, A. 2015, MNRAS, 448, 3248
Girichidis, P., Naab, T., Hanasz, M., & Walch, S. 2018, MNRAS, 479, 3042
Girichidis, P., Naab, T., Walch, S., et al. 2016, ApJL, 816, L19
Górski, K. M., Hivon, E., Banday, A. J., et al. 2005, ApJ, 622, 759
Gronke, M., Bull, P., & Dijkstra, M. 2015, ApJ, 812, 123
Gronke, M., & Dijkstra, M. 2016, ApJ, 826, 14
Gronke, M., Girichidis, P., Naab, T., & Walch, S. 2018, ApJL, 862, L7
Grudić, M. Y., Hopkins, P. F., Faucher-Giguère, C.-A., et al. 2018, MNRAS, 475, 3511
Guo, Y., Bacon, R., Wisotzki, L., et al. 2024, A&A, 691, A66
Haardt, F., & Madau, P. 1996, ApJ, 461, 20
Haiman, Z., Spaans, M., & Quataert, E. 2000, ApJL, 537, L5
Hashimoto, T., Garel, T., & Guiderdoni, B. 2017, A&A, 608, A10
Hayes, M., Östlin, G., Schaerer, D., et al. 2013, ApJL, 765, L27
Hennebelle, P., & Iffrig, O. 2014, A&A, 570, A81
Hopkins, P. F., Chan, T. K., Squire, J., et al. 2021, MNRAS, 501, 3663
Hopkins, P. F., Quataert, E., & Murray, N. 2011, MNRAS, 417, 950
Hopkins, P. F., Wetzel, A., Kereš, D., et al. 2018, MNRAS, 480, 800
Hummels, C. B., Smith, B. D., Hopkins, P. F., et al. 2019, ApJ, 882, 156
Hummels, C. B., Smith, B. D., & Silvia, D. W. 2017, ApJ, 847, 59
Inoue, A. K., Shimizu, I., Iwata, I., & Tanaka, M. 2014, MNRAS, 442, 1805
Izotov, Y. I., Schaerer, D., Worseck, G., et al. 2018a, MNRAS, 474, 4514
Izotov, Y. I., Schaerer, D., Worseck, G., et al. 2021, MNRAS, 503, 1734
Izotov, Y. I., Thuan, T. X., Guseva, N. G., & Liss, S. E. 2018b, MNRAS, 473, 1956
Izotov, Y. I., Worseck, G., Schaerer, D., et al. 2018c, MNRAS, 478, 4851
Joung, M. K. R., & Mac Low, M.-M. 2006, ApJ, 653, 1266
Kakiichi, K., & Gronke, M. 2021, ApJ, 908, 30
Kang, C., Kimm, T., Han, D., et al. 2025, A&A, 693, A149
Katz, H., Liu, S., Kimm, T., et al. 2022, arXiv:2211.04626
Kim, C.-G., & Ostriker, E. C. 2018, ApJ, 853, 173
Kim, J.-G., Gong, M., Kim, C.-G., & Ostriker, E. C. 2023, ApJS, 264, 10
Kim, J.-G., Kim, W.-T., & Ostriker, E. C. 2018, ApJ, 859, 68
Kimm, T., Bieri, R., Geen, S., et al. 2022, ApJS, 259, 21
Kimm, T., Blaizot, J., Garel, T., et al. 2019, MNRAS, 486, 2215
Kimm, T., Cen, R., Devriendt, J., Dubois, Y., & Slyz, A. 2015, MNRAS, 451, 2900
Kimm, T., Haehnelt, M., Blaizot, J., et al. 2018, MNRAS, 475, 4617
Kimm, T., Katz, H., Haehnelt, M., et al. 2017, MNRAS, 466, 4826
Kusakabe, H., Verhamme, A., Blaizot, J., et al. 2022, A&A, 660, A44
Lao, B.-X., & Smith, A. 2020, MNRAS, 497, 3925
Laursen, P., Sommer-Larsen, J., & Andersen, A. C. 2009, ApJ, 704, 1640
Leclercq, F., Bacon, R., Wisotzki, L., et al. 2017, A&A, 608, A8
Li, H., Gnedin, O. Y., & Gnedin, N. Y. 2018, ApJ, 861, 107
Martin-Alvarez, S., Slyz, A., Devriendt, J., & Gómez-Guijarro, C. 2020, MNRAS, 495, 4475
Matthee, J., Sobral, D., Hayes, M., et al. 2021, MNRAS, 505, 1382
Mauerhofer, V., Verhamme, A., Blaizot, J., et al. 2021, A&A, 646, A80
Michel-Dansac, L., Blaizot, J., Garel, T., et al. 2020, A&A, 635, A154
Mitchell, P. D., Blaizot, J., Cadiou, C., et al. 2021, MNRAS, 501, 5757
Morlino, G., & Caprioli, D. 2012, A&A, 538, A81
Murray, N., Quataert, E., & Thompson, T. A. 2005, ApJ, 618, 569
Naab, T., & Ostriker, J. P. 2017, ARA&A, 55, 59
Naidu, R. P., Matthee, J., Oesch, P. A., et al. 2022, MNRAS, 510, 4582
Nebrin, O., Smith, A., Lorinc, K., et al. 2025, MNRAS,
Nelson, D., Pillepich, A., Springel, V., et al. 2019, MNRAS, 490, 3234
Nuñez-Castiñeyra, A., Grenier, I. A., Bournaud, F., et al. 2022, arXiv:2205.08163
Orlitová, I., Verhamme, A., Henry, A., et al. 2018, A&A, 616, A60
Ostriker, E. C., McKee, C. F., & Leroy, A. K. 2010, ApJ, 721, 975
Padoan, P., Pan, L., Haugbølle, T., & Nordlund, Å 2016, ApJ, 822, 11
Pandya, V., Fielding, D. B., Anglés-Alcázar, D., et al. 2021, MNRAS, 508, 2979
Peeples, M. S., Corlies, L., Tumlinson, J., et al. 2019, ApJ, 873, 129
Pillepich, A., Springel, V., Nelson, D., et al. 2018, MNRAS, 473, 4077
Powell, L. C., Slyz, A., & Devriendt, J. 2011, MNRAS, 414, 3671
Prochaska, J. X., Werk, J. K., Worseck, G., et al. 2017, ApJ, 837, 169
Rauch, M., Haehnelt, M., Bunker, A., et al. 2008, ApJ, 681, 856
Rey, M. P., Katz, H. B., Cameron, A. J., Devriendt, J., & Slyz, A. 2024, MNRAS, 528, 5412
Rivera-Thorsen, T. E., Hayes, M., Östlin, G., et al. 2015, ApJ, 805, 14
Rodríguez Montero, F., Martin-Alvarez, S., Slyz, A., et al. 2024, MNRAS, 530, 3617
Roman-Duval, J., Jenkins, E. B., Tchernyshyov, K., et al. 2022, ApJ, 928, 90
Rosdahl, J., Blaizot, J., Aubert, D., Stranex, T., & Teyssier, R. 2013, MNRAS, 436, 2188
Rosdahl, J., Katz, H., Blaizot, J., et al. 2018, MNRAS, 479, 994
Rosdahl, J., Schaye, J., Teyssier, R., & Agertz, O. 2015, MNRAS, 451, 34
Runnholm, A., Gronke, M., & Hayes, M. 2021, PASP, 133, 034507
Ruszkowski, M., Yang, H. Y. K., & Zweibel, E. 2017, ApJ, 834, 208
Salem, M., & Bryan, G. L. 2014, MNRAS, 437, 3312
Saxena, A., Pentericci, L., Ellis, R. S., et al. 2022, MNRAS, 511, 120
Semenov, V. A., Kravtsov, A. V., & Caprioli, D. 2021, ApJ, 910, 126
Seon, K.-i., & Kim, C.-G. 2020, ApJS, 250, 9
Skinner, M. A., & Ostriker, E. C. 2015, ApJ, 809, 187
Smith, A., Bromm, V., & Loeb, A. 2017, MNRAS, 464, 2963
Smith, A., Kannan, R., Garaldi, E., et al. 2022, MNRAS, 512, 3243
Smith, A., Ma, X., Bromm, V., et al. 2019, MNRAS, 484, 39
Song, H., Seon, K.-I., & Hwang, H. S. 2020, ApJ, 901, 41
Stanway, E. R., Eldridge, J. J., & Becker, G. D. 2016, MNRAS, 456, 485

Steidel, C. C., Bogosavljević, M., Shapley, A. E., et al. 2011, ApJ, 736, 160
Steidel, C. C., Erb, D. K., Shapley, A. E., et al. 2010, ApJ, 717, 289
Suresh, J., Nelson, D., Genel, S., Rubin, K. H. R., & Hernquist, L. 2019, MNRAS, 483, 4040
Teyssier, R. 2002, A&A, 385, 337
Trainor, R. F., Steidel, C. C., Strom, A. L., & Rudie, G. C. 2015, ApJ, 809, 89
Veilleux, S., Cecil, G., & Bland-Hawthorn, J. 2005, ARA&A, 43, 769
Verhamme, A., Orlitová, I., Schaerer, D., & Hayes, M. 2015, A&A, 578, A7
Verhamme, A., Orlitová, I., Schaerer, D., et al. 2017, A&A, 597, A13
Verhamme, A., Schaerer, D., & Maselli, A. 2006, A&A, 460, 397
Werk, J. K., Prochaska, J. X., Thom, C., et al. 2013, ApJS, 204, 17
Wisotzki, L., Bacon, R., Blaizot, J., et al. 2016, A&A, 587, A98
Wisotzki, L., Bacon, R., Brinchmann, J., et al. 2018, Natur, 562, 229
Yang, H., Malhotra, S., Gronke, M., et al. 2016, ApJ, 820, 130
Yuan, Y., Martin-Alvarez, S., Haehnelt, M. G., Garel, T., & Sijacki, D. 2024, MNRAS, 532, 3643